

Structures of the Amyloid β -Peptides $A\beta_{1-40}$ and $A\beta_{1-42}$ as Influenced by pH and a D-Peptide

Olujide O. Olubiyi^{†,‡} and Birgit Strodel*,^{†,§}

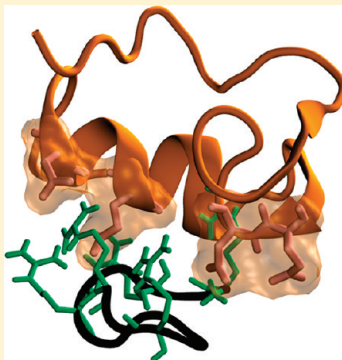
[†]Institute of Complex Systems: Structural Biochemistry, Research Centre Jülich, Germany

[‡]German Research School for Simulation Sciences GmbH, 52425 Jülich, Germany

[§]Institute of Theoretical and Computational Chemistry, Heinrich Heine University Düsseldorf, Universitätsstrasse 1, 40225 Düsseldorf, Germany

Supporting Information

ABSTRACT: In this simulation study, we present a comparison of the secondary structure of the two major alloforms of the Alzheimer's peptide ($A\beta_{1-40}$ and $A\beta_{1-42}$) on the basis of molecular dynamics (MD) simulations on the microsecond time scale using the two GROMOS96 force fields ffG43a2 and ffG53a6. We observe peptide and force-field related differences in the sampled conformations of $A\beta_{1-40}$ and $A\beta_{1-42}$, which we characterize in terms of NMR chemical shifts calculated from the MD trajectories and validate against the corresponding experimental NMR results. From this analysis, we can conclude that ffG53a6 is better able to model the structural propensities of $A\beta_{1-40}$ and $A\beta_{1-42}$ than ffG43a2. Furthermore, we provide a description of the influences of pH and binding of D3, a 12-residue D-enantiomeric peptide with demonstrated antiamyloid effects, on the structure of $A\beta_{1-42}$. We demonstrate that, under slightly acidic conditions, protonation of the three histidine residues in $A\beta_{1-42}$ promotes the formation of β -sheets via a reduction in electrostatic repulsion between the two terminal regions. Our studies further reveal that the binding between D3 and $A\beta_{1-42}$ is driven by electrostatic interactions between negatively charged $A\beta_{1-42}$ residues and the five positively charged arginine residues of D3. The binding of D3 was found to induce large conformational changes in the amyloid peptide, with a reduction in β -sheet units being the most significant effect recorded, possibly explaining the observed amyloid-inhibiting properties of the D-peptide.



1. INTRODUCTION

Protein folding abnormalities are an important class of pathogenic causes of diseases such as Alzheimer's and Parkinson's diseases, and diabetes mellitus. In Alzheimer's disease (AD), post-translational cleavage products of the amyloid precursor protein (APP) have been identified as a clinical hallmark in disease development and progression. The small-molecular-weight amyloid- β ($A\beta$) peptide, which is released as a result of APP enzymatic cleavage, undergoes conformational transitions from a predominantly helical fold adopted in the hydrophobic transmembrane environment to structural states in the aqueous extracellular medium that currently constitute the subject of intensive research. Of the proteolytic cleavage products of APP, which typically contain 39–43 residues, $A\beta_{1-42}$ is recognized as the most important alloform, primarily on the basis of roles in eliciting neurotoxicity. Conformational transition of the extracellular $A\beta$ peptide to a β -sheet-rich state, resulting in its aggregation into water-soluble oligomers is believed to be crucial in the initiation of Alzheimer's dementia.¹ Recent evidence suggests that the water-soluble oligomers rather than the fibrils are responsible for the toxicity observed in Alzheimer's patients.² Plaque deposition does not correlate well with pathogenicity and disease progression, but on the other hand, both dimers and trimers obtained from Alzheimer's brains were demonstrated to

affect "synaptic plasticity" and long-term potentiation,³ and fibril structures were shown to be one of the least toxic species in cultured neurons.⁴

The rapid aggregation tendency of $A\beta$ has made access to structural information under physiological conditions highly challenging. Attempts to circumvent this problem include the use of apolar solvents in preparing samples for NMR experiment.^{1,5–8} Under these conditions $A\beta_{1-42}$ was shown to consist of two helical regions separated by a turn structure.¹ Molecular dynamics (MD) studies reported extensive structural changes on immersing this helical structure in completely aqueous medium, involving rapid loss of the C-terminal helix and a conversion of the N-terminal helix from α - to π -helix.¹ In general, both regions of the peptide have been shown to sample a wide range of conformations from β -sheets to random coil and helical structures. A structural model developed recently using NMR ¹⁵N relaxation data for probing the persistence length of $A\beta_{1-40}$ suggested that rather than being wholly disordered at physiologically relevant temperatures, the secondary structures sampled by the $A\beta$ peptide are overshadowed by thermal motions, making it difficult to directly

Received: August 9, 2011

Revised: January 27, 2012

Published: February 2, 2012

probe it in experiments.⁹ The secondary structures could be better observed at lower temperatures (3–13 °C), resulting in a model for $A\beta_{1-40}$ consisting of π -helices for residues 1–4 and 11–15 and β -sheets for residues 16–24 and 31–40, separated by unstructured residues in between.

Molecular simulations offer a direct means of accessing the conformational states of the $A\beta$ peptides in aqueous media.^{10–13} MD studies have suggested that $A\beta$ peptides, rather than being entirely disordered, are usually able to sample sequence-specific secondary structures.^{14–19} Using chemical shifts calculated from replica exchange molecular dynamics simulations, Wood and Rothlisberger investigated the differences observed between theoretical studies and experiments.²⁰ They showed that the assigned random coil structures often derive from an averaging of β -sheet, α -helical and random coil structures.

Various studies (using NMR or MD) have also attempted to identify distinctions in the secondary structure and aggregation patterns of the two major $A\beta$ alloforms: $A\beta_{1-40}$ and $A\beta_{1-42}$.^{15,21} The extra two residues of the latter peptide were found to confer higher rigidity on its C-terminal, which may explain the higher amyloidogenicity and thus neurotoxicity observed for this peptide.²¹ Yang and Teplow contended that rather than being unstructured, the two peptides possess a “unique statistical coil” with distinct folding units separated by turns.¹⁶ They observed the extra residues of $A\beta_{1-42}$ as increasing C-terminal contact with the central hydrophobic core (CHC), thereby significantly stabilizing the β -sheet structure more than in $A\beta_{1-40}$, in which the CHC would rather interact with the N-terminal segment.

The aggregation of $A\beta$ monomers into toxic β -sheet-rich oligomer structures is believed to depend to a significant extent on the sampled conformational state of the monomer and factors influencing it. Metal ions, such as Cu^{2+} , Zn^{2+} , and Fe^{2+} , lipid membranes, the presence of preformed oligomers, and hydrogen ion homeostasis have been found to influence the aggregation kinetics.^{22–25} Acidic pH was suggested to be an important factor promoting amyloid aggregation.²² The protonation state of $A\beta$ histidine residues (His6, His13, and His14) is strongly influenced by pH changes with a change in net molecular charge from –3 to 0 associated with a change from neutral to slightly acidic pH values. It was found that pH-controlled structural changes can also be attributed to metal ion-binding and to changes in the electrostatic charge distribution of the molecule.²⁴ For instance, the binding of Cu^{2+} by $A\beta_{1-28}$ was observed to be pH-dependent, with the divalent metal ion inducing aggregation only at pH values lower than the physiological pH.²³ Whether it is by promoting metal coordination or by intrinsic redistribution of electrostatic charges, acidic pH values are likely to promote amyloid aggregation by decreasing the hydrophilicity of the N-terminal portion of $A\beta$. Given the slightly acidic nature of accompanying inflammatory response in AD,²⁶ acidic pH-facilitated aggregation is likely to be of importance in disease development. It has been shown that brains from patients who die from AD are more acidic than brains from patients who die suddenly with no brain disease.²⁷

The molecular events surrounding its causative role in AD make $A\beta$ a viable target for drug discovery purpose. Different therapeutic strategies exploiting conformational aspects of $A\beta$ have been employed.^{28,29} High-throughput screening of chemical libraries identified small compound inhibitors of amyloid aggregation.^{30,31} Immunotherapeutic approaches con-

stitute an important approach involving the use of both active and passive immunization for clearing endogenous $A\beta$.^{32,33} Rational drug discovery approaches employ peptides and derivatives synthesized based on the self-recognition unit $^{16}KLVFF$ ²⁰ of the $A\beta$ peptide.^{29,34}

Insertion of a bulky group or proline as β -sheet breaker within the self-recognition-derived peptide sequence has also been demonstrated as effective in inhibiting amyloid aggregation.^{35–40} Furthermore, peptidic inhibitors were also reported that via stabilization of the helical structure in residues 13–23 of $A\beta$ prevented the formation of neurotoxic aggregates.³⁹ Peptide drugs, however, suffer from a significant drawback; that is, the fast rate at which they are cleared from circulation by endogenous peptidases. Approaches employed in circumventing this disadvantage include the use of D-enantiomeric peptides. D-Peptides have been identified as inhibitors of amyloid formation and cytotoxicity of the $A\beta$ peptide.^{40–46} D-Peptides containing some matching amino acid sequence in the key amyloidogenic motif of $A\beta$, $^{16}KLVFFA$ ²¹, were shown to be effective in inhibiting fibrillogenesis while at the same time being more protease-resistant and less immunogenic than L-peptides.⁴³ Recently, a 12-residue arginine-rich D-peptide called D3 (sequence RPRTRL-HTHRNR) was identified by mirror-image phage display⁴⁴ and was shown to reduce $A\beta$ plaque load and cognitive deficits in transgenic mice in vivo.^{45,46} In addition, it also specifically precipitates toxic $A\beta$ oligomers into nontoxic nonamyloidogenic amorphous aggregates in vitro.⁴⁴

In this study, we use multiple MD simulations on a microsecond time scale in explicit water to study various influences on the secondary structure of the $A\beta$ peptide. We present a perspective on the intramolecular effects of the histidine protonation state on the sampled structures of $A\beta_{1-42}$ and how this may be the basis for its increased aggregation kinetics at acidic pH. We also compare the secondary structure of $A\beta_{1-40}$ and $A\beta_{1-42}$ using two GROMOS96 force fields, which increases the likelihood of discriminating peptide-dependent dynamics from force field effects. We evaluate the performance of the two force fields by calculating NMR chemical shifts from the MD trajectories of $A\beta_{1-40}$ and $A\beta_{1-42}$ and compare the calculated values to the corresponding experimental chemical shift results. Using the insights afforded by $A\beta$ conformational studies, we proceed to investigate the reported antiamyloid properties of D3. To unravel D3's mechanism of amyloid aggregation inhibition, we employ a combination of a global optimization method^{47–50} and MD simulations.

2. EXPERIMENTAL METHODS

2.1. Structural Models.

Initial coordinates for the D3 peptide were generated using the Dundee PRODRG2 server⁵¹ and parameters derived from the force fields employed for the MD simulations. Solution NMR structures PDB 1BA4 and 1Z0Q for $A\beta_{1-40}$ and $A\beta_{1-42}$, respectively, were taken from the RCSB Protein Data and employed as starting configurations for the MD simulations (Figure 1). Protonation states for ionizable residues in both D3 and $A\beta$ peptides were chosen for a physiological pH, with both arginine and lysine residues modeled as positively charged and glutamic and aspartic acids as deprotonated. If not otherwise stated, histidine residues were modeled as neutral with only the δ nitrogen protonated. The N and C termini were chosen to be protonated and deprotonated, respectively, in both D3 and $A\beta$ peptides to mimic the physiological states at pH 7.4.

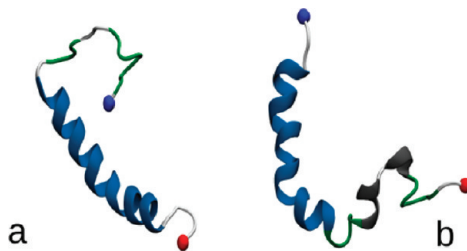


Figure 1. $\text{A}\beta$ starting structures: (a) $\text{A}\beta_{1-40}$ (PDB 1BA4), (b) $\text{A}\beta_{1-42}$ (PDB 1Z0Q). The N and C termini are represented as blue and red beads, respectively.

2.2. Molecular Dynamics Simulations. In this study, four 1.5 μs , two 1.0 μs , and three 335 ns MD simulations of $\text{A}\beta$, 100 10 ns MD simulations of $\text{A}\beta/\text{D}3$ complexes, and one 100 ns MD simulation of D3 were performed. In the following, we describe the 100 ns simulation of D3 using the GROMOS ffG43a2 force field.^{52,53} The peptide was centered in a cubic simulation box with a 1 nm distance allowed between the peptide and the edges of the box treated with periodic boundary conditions. The particle mesh Ewald method was employed for treating long-range electrostatics with a 1.4 nm cutoff for calculating short-range forces. After steepest descent energy minimization in vacuo, the box was solvated with the SPC explicit water model, and Na^+ and Cl^- ions were added to obtain a NaCl concentration of 150 mM and to achieve charge neutrality. The solvated peptide was then minimized using both steepest descent and conjugate gradient energy minimization methods. With a restraining force of 1000 kJ/mol on the positions of all non-hydrogen atoms of D3, we performed a 1 ns equilibration dynamics (NPT) in which the water molecules were allowed to equilibrate around the restrained peptide atoms, in the process removing bad contacts and bringing the system near equilibrium conditions for the subsequent production MD run. For the equilibration step, the system was coupled to a Berendsen thermostat and barostat. The restraints were subsequently turned off, and a 100 ns production run was performed at 300 K in an NPT ensemble with temperature and pressure modulated by coupling to a Nosé–Hoover thermostat and a Parrinello–Rahman barostat, respectively. The neighbor list was generated every 10 ps, with a cutoff of 1.4 nm, and coordinates were saved every 20 ps.

The procedure followed for the preparation of the MD simulation of D3 was also employed for the MD simulations of $\text{A}\beta_{1-40}$ and $\text{A}\beta_{1-42}$. Both peptides were simulated using two GROMOS force fields, ffG43a2^{52,53} and ffG53a6,⁵⁴ giving rise to four simulations in this phase of the study. After the initial 1 ns equilibration, the production MD runs were performed for 1.5 μs in each system. To investigate the effect of histidine protonation state on $\text{A}\beta_{1-42}$ folding, we separately performed two 1 μs MD simulations (ffG43a2 and ffG53a6) with the three histidine residues of $\text{A}\beta_{1-42}$ protonated on both imidazolyl nitrogen atoms. In addition, from the 1.5 μs MD simulation of $\text{A}\beta_{1-42}$ with neutral histidine residues (ffG43a2), three frames dumped at 713, 817, and 888 ns were each subjected to further 335 ns MD simulations (totaling $\sim 1 \mu\text{s}$). These MD simulations were used as reference for quantifying the effect of D3 binding on the secondary structural features of $\text{A}\beta_{1-42}$. MD simulations performed for $\text{A}\beta_{1-42}/\text{D}3$ complexes are discussed below. All the MD simulations were performed with the GROMACS 4.5 program.⁵⁵

2.3. Basin-Hopping Global Optimization. The basin-hopping (BH) approach to global optimization^{47,48} is analogous in principle to the Monte Carlo-minimization approach.⁵⁰ Moves are proposed by perturbing the current geometry and are accepted or rejected on the basis of the energy difference between the local minimum obtained by minimization from the instantaneous configuration and the previous minimum in the chain. In effect, the potential energy surface is transformed into the basins of attraction of all the local minima so that the energy for configuration \mathbf{r} is

$$\tilde{E}(\mathbf{r}) = \min\{E(\mathbf{r})\}$$

where “min” denotes minimization. Large steps can be taken to sample this transformed landscape, since the objective is to step between local minima. Furthermore, there is no need to maintain detailed balance when taking steps because the BH approach attempts to locate the global potential energy minimum and is not intended to sample thermodynamic properties. The BH algorithm has been implemented in the GMIN program.⁵⁶ We used the oligomer-generation procedure⁴⁹ in GMIN to generate 6000 $\text{A}\beta_{1-42}/\text{D}3$ complexes from three different $\text{A}\beta_{1-42}$ structures and the most favored structure of D3. After their initial generation, the complexes were optimized using 500 BH steps with dihedral angle moves⁵⁷ and small rigid body rotations and translations⁵⁸ applied to D3. Dihedral angles were twisted up to a maximum of 20° with a probability of 20%, and rigid body rotation and translation were conducted at a maximum of 60° and 2 Å, respectively. All the systems were treated with the parameters from the CHARMM22 force field.⁵⁹ The different force field choices for our MD and GMIN simulations are due to the fact that the GROMOS force fields are not interfaced to GMIN, and the CHARMM potential was not yet implemented in GROMACS at the time of this study.

Upon completion, the lowest-energy structure from each BH run was saved and selected for MD refinement on the basis of the intermolecular separation and energy cutoffs. For the separation between $\text{A}\beta_{1-42}$ and D3, we applied a cutoff of 10 Å between their centers of mass, and for the energies, we required them to be below -1850 kcal/mol with the CHARMM22 potential. With these thresholds, we obtained 313 structures, from which 100 structures were selected with care taken to ensure that the three $\text{A}\beta_{1-42}$ starting structures employed for the BH runs were equally represented. Each of these 100 $\text{A}\beta_{1-42}/\text{D}3$ complexes was subjected to 10 ns MD (totaling 1 μs) simulation in explicit solvent using the GROMOS ffG43a2 force field^{52,53} following a protocol analogous to that described above for $\text{A}\beta_{1-42}$ with neutral histidine residues.

3. RESULTS AND DISCUSSION

We initiated our MD simulations to study the structural propensities of $\text{A}\beta_{1-40}$ and $\text{A}\beta_{1-42}$ from the solution NMR models shown in Figure 1. The structure for $\text{A}\beta_{1-40}$ was solved in aqueous sodium dodecyl solvate micelles at pH 5.1 and consists of an α -helix between residues 15 and 36 (PDB 1BA4).⁷ The $\text{A}\beta_{1-42}$ structure has two α -helices between residues 10 and 32 and was determined in a hexafluoroisopropyl alcohol/water mixture (PDB 1Z0Q).¹ For each peptide, we set up two 1.5 μs MD simulations using the GROMOS force fields ffG43a2^{52,53} and ffG53a6.⁵⁴

3.1. Secondary Structure of $\text{A}\beta_{1-40}$. The secondary structure transitions in each of the two 1.5 μs MD simulations were monitored using DSSP, a program that uses hydrogen

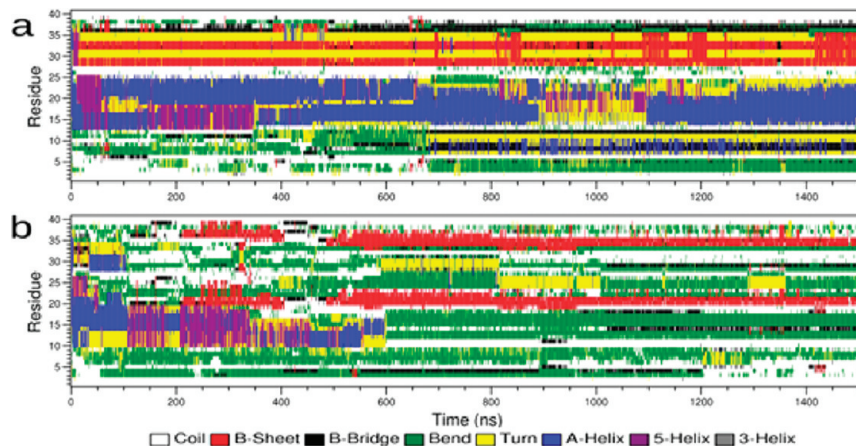


Figure 2. DSSP plots for secondary structure transitions in A β ₁₋₄₀ during 1.5 μ s MD simulations using the GROMOS forcefields (a) ffG43a2 and (b) ffG53a6.

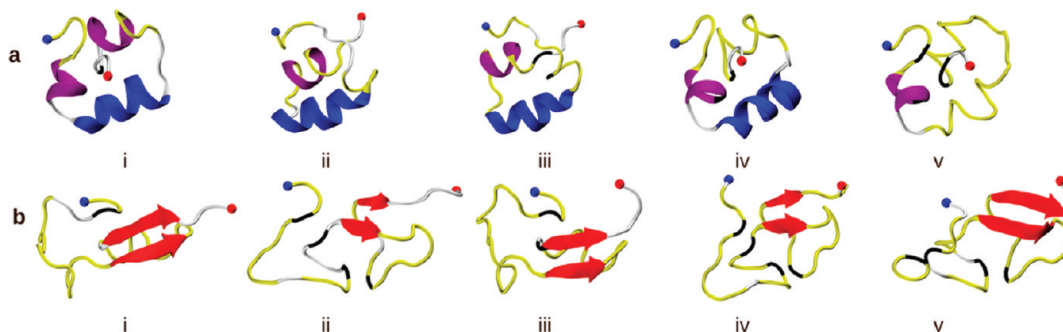


Figure 3. A β ₁₋₄₀ structures for the centers of the five most populated clusters obtained from the last 1000 ns of the MD simulations with (a) ffG43a2 and (b) ffG53a6. The cluster size decreases from i to v. All graphics were generated using VMD.⁶⁰ The peptide is colored according to secondary structure: red for β -sheet, blue for α -helix, purple for π -helix, green for bend, yellow for turn, and white for coil structure. The N and C termini are represented as blue and red beads, respectively.

bond and geometric pattern recognition for secondary structure assignment.⁶⁰ According to the DSSP plot for ffG43a2 (Figure 2a), the N-terminal α -helix was largely retained, whereas the short C-terminal helix was rapidly (within 20 ns) converted to β -sheets and turns. Partial conversion of the α -helix (N-terminal region) to a π -helix was recorded between 20 and 90 ns for residues 13–25 and between 140 and 340 ns involving residues 13–18. Compared with the other sections of the peptide, residues 13–25 appear to have a higher helix-forming propensity capable of existing in either the α - or π -helical form. Only between 900 and 1100 ns did this sequence not adopt a helical conformation; instead, it was largely disordered, involving turn structures. Throughout the 1.5 μ s trajectory, the N-terminal residues 1–14 mostly exist in a disordered state with some secondary structures, especially α -helix and β -bridge, transiently sampled in the second half of the simulation. The C-terminal residues 28–39 consistently sampled β -conformations with residues 30–31 and 34–35 mainly existing as turns. A three-residue random coil stretch starting with Gly25 separates the β -rich C-terminal segment from the helix-forming CHC.

The conformational changes observed in the ffG53a6 simulation of A β ₁₋₄₀ (Figure 2b) reveal some distinctions from those observed in the ffG43a2 simulation. With ffG53a6, the helix in the CHC is not stable and was sustained for only the first 600 ns of the MD simulation. Furthermore, this helix involved fewer participating residues, but included the N-terminal residues 10–14. During the initial 200 ns, the C-terminal section of A β ₁₋₄₀ undergoes rapid structural

conversions into helix, β -sheets, and disordered states. From 200 ns until the end of the simulation, a β -sheet was sampled between the C-terminal residues 32–37 and residues 19–23, with the mediating residues 24–31 mostly sampling disordered states. A slight propensity for β -strand was also demonstrated for the N-terminal residues; otherwise, the N-terminal residues 1–10 (up to 600 ns) and 1–17 (between 600 ns and 1.5 μ s) sampled mostly coil structures. In general, the DSSP plot for ffG53a6 indicates a higher structural flexibility for A β ₁₋₄₀ than for ffG43a2, for which the secondary structural pattern sampled by different sections of the peptide was mostly sustained for the duration of the simulation.

To better describe the conformational behavior predicted by the two force fields, we clustered the sampled configurations in each trajectory on the basis of the method by Daura et al.,⁶¹ which uses a 0.2 nm cutoff for the backbone atoms. Here, we have used the last 1.0 μ s of the trajectories only, that is, from 500 ns to 1.5 μ s, at which time we observed a certain level of conformational equilibrium (also according to chemical shift values discussed in section 3.4). The representative structures for the five most populated clusters are shown in Figure 3. The cluster centers capture the pattern of structural changes shown in the DSSP plots in Figure 2. It is noteworthy, however, that for the ffG43a2 results (Figure 3a), the visualization program VMD⁶² assigns a π -helix to the C-terminal region, whereas DSSP found a strand-turn-strand-turn motif between residues 28 and 36. The five main clusters contain 94% and 26% of the total number of structures sampled in the ffG43a2 and ffG53a6

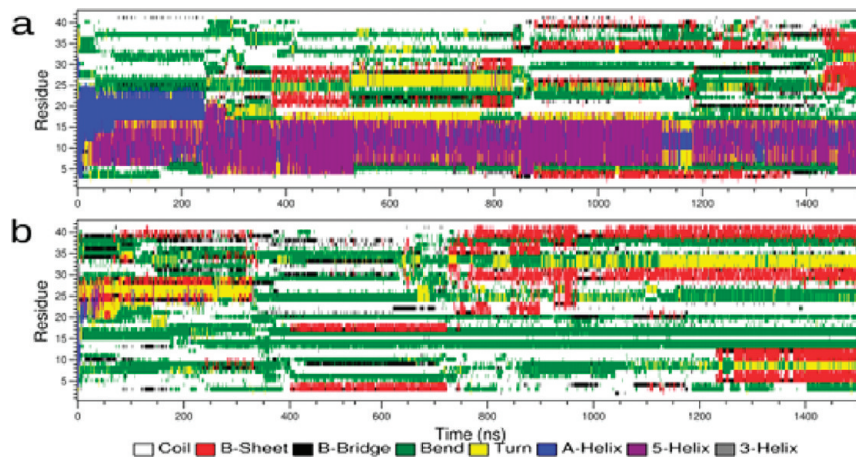


Figure 4. DSSP plots for secondary structure transitions in A β ₁₋₄₂ during 1.5 μ s MD simulations using the GROMOS forcefields (a) ffG43a2 and (b) ffG53a6.

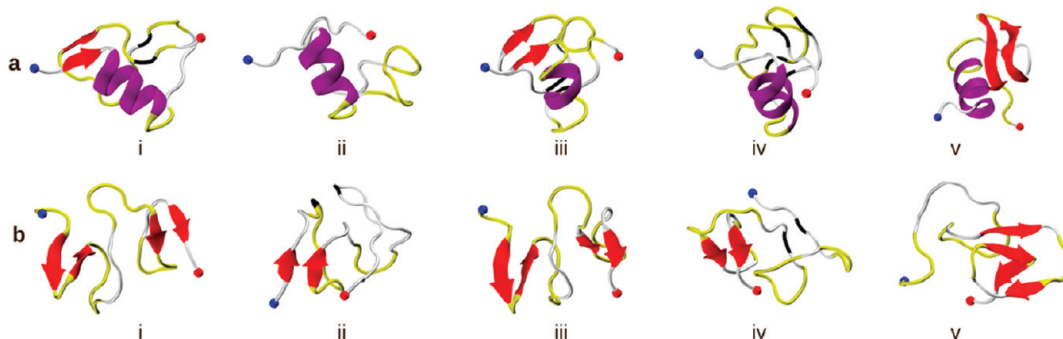


Figure 5. A β ₁₋₄₂ structures for the centers of the five most populated clusters obtained from the last 1000 ns of the MD simulations with (a) ffG43a2 and (b) ffG53a6. The cluster size decreases from i to v. See Figure 3 for explanation of colors.

simulations, respectively. This indicates that A β ₁₋₄₀ experiences a higher conformational flexibility with the ffG53a6 force field, the N-terminal region in particular, than with ffG43a2. The five cluster centers for ffG43a2 feature a predominantly helical conformation separated by coils and to a much lesser extent, turns. With ffG53a6, the cluster centers are characterized by a disordered N-terminal segment and a β -sheet involving the two sequence stretches ¹⁹FAED²³ (part of the CHC self-recognition sequence) and ³²IGLMVG³⁷ (part of the C-terminal hydrophobic region). The terminal ³⁸GVV⁴⁰ is disordered in all five clusters, as supported by the DSSP plot in Figure 2b.

The results of the simulations, especially those from the ffG53a6 simulation, partly agree with the structural model proposed from ¹⁵N relaxation data.⁹ From persistence length measurements obtained at temperatures between 3 and 18 °C, a model composed of six structural units was suggested for monomeric A β ₁₋₄₀: π -helix for residues 1–4, unstructured residues 5–10, π -helix for residues 11–15, β -strand for residues 16–24, unstructured residues 25–30, and β -strand for residues 31–40. With ffG53a6, we also observed unstructured regions involving residues 1–18 and 24–31 in partial agreement with the proposed experimental model. Furthermore, the β -sheet between residues 19–23 (16–24 in the experimental model) and 32–37 (31–40 in the model) also agrees with the NMR relaxation model.⁹ Only the π -helices for residues 1–4 and 11–15 are not found to be stable in our ffG53a6 simulation of A β ₁₋₄₀.

3.2. Secondary Structure of A β ₁₋₄₂. The secondary structure of A β ₁₋₄₂ resulting from the DSSP analysis of the

trajectories for the two force fields under study is shown in Figure 4. The DSSP plot for ffG43a2 shows a similar pattern of a stable N-terminal helix, as observed for A β ₁₋₄₀, but in this case, it is dominated by a π -helix between residues 5–15. Residues 20–30 sample a sheet-bend/turn-sheet conformation between 370 and 840 ns, after which this segment became disordered and the sheet structure shifted to residues 33–40 and 2–4 in the N-terminus. With ffG53a6, the two helical units in the initial structure were completely lost within 100 ns. Despite the high conformational flexibility suggested by the DSSP plot (Figure 4b), different conformational motifs can be observed with the system temporally divided into four stages on the basis of sampled β -sheet/random coil states. In the first 400 ns, residues 24–40 intermittently but continually sample a β -sheet structure, and residues 1–23 are mostly disordered. Between 400 and 725 ns, a β -sheet exists in the N-terminal region, and both the CHC and the C-terminal sections sample disordered states. Beyond 725 ns, the C-terminal region adopts a β -sheet conformation, and the N-terminal section is disordered until 1250 ns. For the last 250 ns of the simulation, a β -sheet is also sampled in the N-terminal region involving residues 6–13.

As for A β ₁₋₄₀, we clustered the sampled conformations from the last microsecond of the MD trajectories. The secondary structure of the cluster centers for the five most populated clusters (Figure 5) reveals a long N-terminal π -helix (residues 4–16) for ffG43a2 and, in contrast to the pattern observed for A β ₁₋₄₀, a β -sheet sampled in residues 20–29 with intervening coil at residues 23–25. This suggests a higher β -sheet

propensity in the longer peptide, given that the force field bias remains constant in both simulations. Similar to the results obtained for $\text{A}\beta_{1-40}$, 76% of the sampled structures are included in the five most populated clusters, indicating that fewer conformational states were sampled by ffG43a2 compared with ffG53a6, in which only 48% of all structures are included in the five main clusters. The cluster centers for ffG53a5 are dominated by β -sheets in residues ³EFRHDSG⁹, the CHC self-recognition unit ¹⁷LVFFAE²², and the C-terminal hydrophobic sequence ³⁰A(II)GLM(VGG)V⁴⁰. The sequences shown in parentheses are the observed intervening disordered states. Residues ³⁶VGG³⁸ have already been identified as uniquely characteristic of $\text{A}\beta_{1-42}$ for forming a hinge structure.⁶³ The MD simulation with ffG53a6 revealed $\text{A}\beta_{1-42}$ as being able to form β -sheets in its N-terminal, midsequence, and the C-terminal segments, as compared with its shorter alloform whose β -sheets formation was confined to the CHC and the C-terminal sections, and this to a much lesser degree.

3.3. Comparison of $\text{A}\beta_{1-40}$ and $\text{A}\beta_{1-42}$. Previous studies conducted on $\text{A}\beta_{1-40}$ and $\text{A}\beta_{1-42}$ revealed certain distinctions in their structures and aggregation properties, even though there are only two extra residues in the C-terminal end of $\text{A}\beta_{1-42}$ ^{63,64} differentiating its primary structure from that of $\text{A}\beta_{1-40}$. Nuclear Overhauser effect (NOE) measurements indicate that both peptides exhibit high conformational interconversion at the pico- to nanosecond time scale with NOE values for the C terminus of $\text{A}\beta_{1-42}$, indicating a higher rigidity compared with $\text{A}\beta_{1-40}$.²¹ This rigidity was proposed to restrict the C-terminal segment of $\text{A}\beta_{1-42}$ to a β -strand conformation suggested to act as an internal seed for amyloid aggregation. Studies by Urbanc et al. identified the presence of a turn at Gly37-Gly38 in $\text{A}\beta_{1-42}$ as an additional feature distinguishing it from $\text{A}\beta_{1-40}$.^{63,64} This turn was suggested as an explanation for the preference of $\text{A}\beta_{1-42}$ toward pentamer and hexamer formation, as against dimeric structures preferentially formed by $\text{A}\beta_{1-40}$.^{63,65,66} They also reported the presence of a β -strand at Ala2-Phe4 exclusively in $\text{A}\beta_{1-40}$.⁶³

From our simulations, we observe that both peptides are mainly unstructured in the first 10 N-terminal residues. However, we find that $\text{A}\beta_{1-40}$ is more disordered in this region than $\text{A}\beta_{1-42}$, which also samples either a π -helix or β -sheet in the N-terminal residues. Both peptides adopt β -sheets in the self-recognition β -forming ¹⁶KLVFF²⁰ motif involving ¹⁷LVFFAE²² in $\text{A}\beta_{1-42}$ (both force fields) and ²⁰FAED²³ in $\text{A}\beta_{1-40}$ (ffG53a6 only). The ¹⁶KLVFF²⁰ motif has been identified as responsible for nucleating aggregation³⁴ and belongs to one of the two hydrophobic stretches (¹⁷LVFFA²¹ and ³⁰AIIGLMVGGVV⁴⁰I⁴²) of amino acid residues present in the two peptides. Our simulations show a conformational separation around residues Gly25-Asn27 between the two hydrophobic units in both peptides in aqueous medium. Both force fields reveal a complete loss of the helical structure in the second hydrophobic stretch in both peptides, which instead prefers β -sheet conformations in water. A conformational transition from helical to coil structure has been suggested as a prerequisite for β -sheet formation and amyloid aggregation.¹ Although both C-terminal segments sampled β -strand conformation, it is only in $\text{A}\beta_{1-42}$ that a Gly37-Gly38 hinge structure was sampled, which is in agreement with earlier studies.^{63,64} The last three residues in the C-terminus of $\text{A}\beta_{1-40}$ sampled random coil. In $\text{A}\beta_{1-42}$, the C-terminal coil is reduced to two residues with Ala40 stably involved in β -sheets, which is

a mild indication of higher C-terminal stiffness in the longer $\text{A}\beta$ peptide.²¹

3.4. Validation of the Simulation Data against Experimental NMR Chemical Shifts. To gain more insight into the convergence of our MD simulations and to validate the force field models, we calculated NMR chemical shifts (δ_{calc} , pH ~ 7, 300 K) and compared them to experimentally determined chemical shifts (δ_{exp} , pH ~ 7, 278 K).⁶⁷ Chemical shifts were calculated for N, HN, C α , and C β atoms using the empirical approach CAMSHIFT, which exploits the dependence of chemical shift on conformation represented as a polynomial expansion of intramolecular distances and was shown to be of performance similar to other empirical shift prediction methods.⁶⁸

We computed the time-averaged root mean-square deviation (rmsd) between δ_{calc} and δ_{exp} for the 1.5 μ s trajectories from the ffG43a2 and ffG53a6 simulations of $\text{A}\beta_{1-40}$ and $\text{A}\beta_{1-42}$ (Table 1). To present the time evolution of the rmsd's, we also

Table 1. Time-Averaged rmsd's between Simulated and Experimental Chemical Shift Values for N, HN, C α , and C β Atoms for the Full-Length (1–1500 ns) and 500 ns Blocks of the MD Trajectories of $\text{A}\beta_{1-40}$ and $\text{A}\beta_{1-42}$

		rmsd [ppm]			
		N	HN	C α	C β
$\text{A}\beta_{1-40}/\text{ffG43a2}$	1–1500 ns	4.05	0.40	1.77	1.08
	1–500 ns	3.95	0.40	1.79	1.09
	500–1000 ns	4.01	0.40	1.76	1.09
	1000–1500 ns	4.19	0.41	1.77	1.07
$\text{A}\beta_{1-42}/\text{ffG43a2}$	1–1500 ns	3.68	0.45	1.54	1.21
	1–500 ns	3.87	0.43	1.69	1.17
	500–1000 ns	3.64	0.46	1.49	1.20
	1000–1500 ns	3.51	0.44	1.43	1.26
$\text{A}\beta_{1-40}/\text{ffG53a6}$	1–1500 ns	3.22	0.34	1.25	1.28
	1–500 ns	3.71	0.35	1.46	1.13
	500–1000 ns	3.08	0.33	1.16	1.27
	1000–1500 ns	2.87	0.34	1.12	1.44
$\text{A}\beta_{1-42}/\text{ffG53a6}$	1–1500 ns	2.96	0.36	1.23	1.24
	1–500 ns	3.40	0.36	1.24	1.22
	500–1000 ns	2.68	0.35	1.30	1.19
	1000–1500 ns	2.74	0.37	1.18	1.30
CAMSHIFT test set ^a		3.01	0.56	1.30	1.36

^aFor comparison, the deviations between experimental and with CAMSHIFT-predicted chemical shifts for a protein test set are provided.⁶⁸

calculated these values for 500 ns blocks of the MD trajectories. A plot of the shift rmsd's versus time can be found in the Supporting Information. In Table 1, we also present the deviations between experimental and predicted chemical shifts for a protein test set.⁶⁸ The data obtained for the four chemical shift types (N, HN, C α , and C β) show that the rmsd values are within or near to the expected deviations, especially for the force field ffG53a6. The rmsd values for $\text{A}\beta_{1-40}$ and $\text{A}\beta_{1-42}$ modeled with ffG43a2 show that this force field is not fully able to reproduce the experimentally determined shift values. Although δ_{calc} for HN and C β are generally consistent with the experimental values (ffG43a2 and ffG53a6), the rmsd's for the amide N and C α shifts reveal that these shifts converge to the experimental values only for the simulations with ffG53a6. With ffG53a6, the average rmsd's for the N and C α shifts are generally below the expected deviation for simulation times

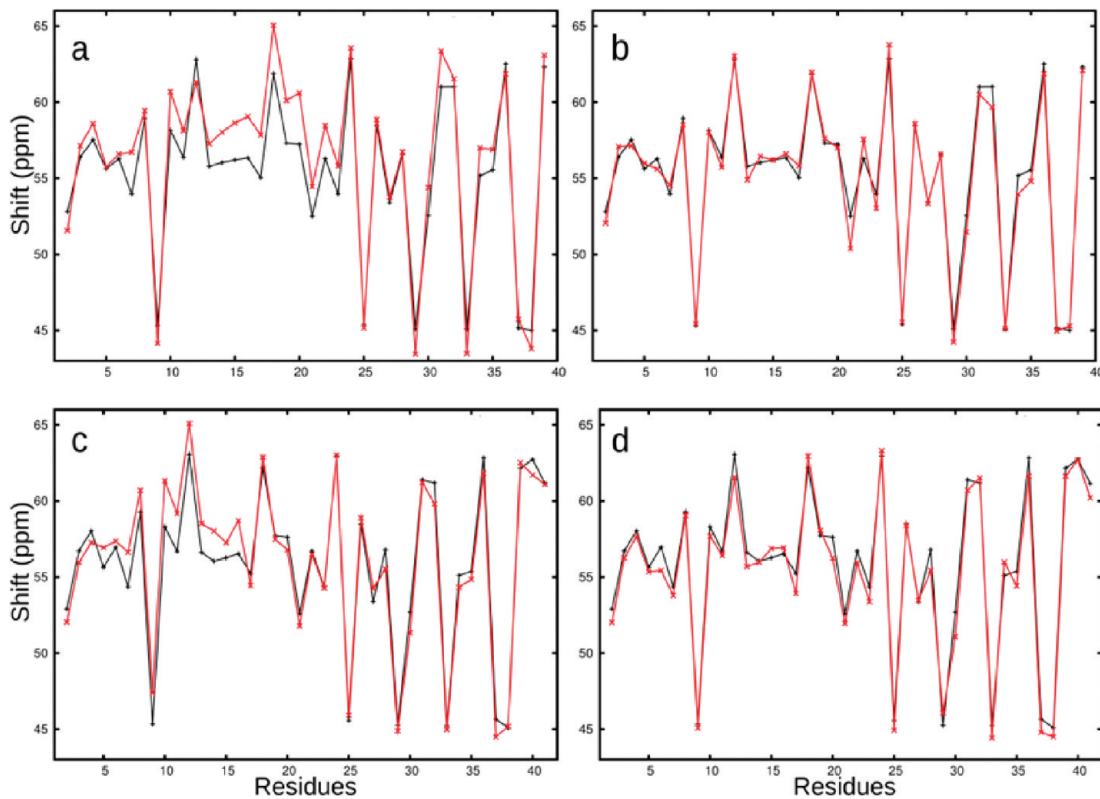


Figure 6. Comparison of simulated and experimental $C\alpha$ chemical shifts. Chemical shift values were calculated using the CAMSHIFT program⁶⁸ following MD simulations at 300 K (red) and were compared with values measured experimentally at 278 K by NMR (black).⁶⁷ The calculated values are time-averaged chemical shifts for the last 1000 ns of the MD simulations for (a) $A\beta_{1-40}$ with ffG43a2, (b) $A\beta_{1-42}$ with ffG43a2, (c) $A\beta_{1-40}$ with ffG53a6, and (d) $A\beta_{1-42}$ with ffG53a6.

larger than 500 ns. Only for $A\beta_{1-40}$ with ffG53a6, the rmsd for the N chemical shift is slightly above 3.01 ppm between 500 and 1000 ns; it decreases to values below 3.01 ppm for simulation times above 600 ns (see the Supporting Information). This decrease in rmsd coincides with the conversion from a helical to coil state in the N-terminal segment around 600 ns (Figure 2b).

In $A\beta_{1-42}$, a transition from coil to β strand is observed for some N-terminal residues around 400 ns (Figure 4b), which causes the rmsd to decrease considerably at this time. This finding supports our approach to use 500 ns as the boundary between the equilibration and the production phases for the analysis of our MD simulations. For the ffG43a2 simulations, however, it becomes evident that the rmsd's do not decrease during the last 1000 ns of the MD trajectories; in some cases, they even increase, showing that this force field does not sample the experimentally observed structures. However, it needs to be noted that the experimental chemical shifts were obtained at 278 K⁶⁷ and our MD simulations were performed at 300 K, which may lead to deviations from the experimental results. Our findings from the comparison with experimental chemical shift values are further confirmed by the comparison of calculated and experimental J -coupling (${}^3J_{\text{HNN}\alpha}$) data, which is presented in the Supporting Information.

To get insight into which of the residues cause the deviation of $\langle \delta_{\text{calc}} \rangle$ from δ_{exp} , we computed for the last 1000 ns of the MD trajectories the average chemical shift values for $C\alpha$, $\langle \delta_{\text{calc}} \rangle$, and plotted these against δ_{exp} in Figure 6. To highlight the deviations between computation and experiment, we calculated the difference between $\langle \delta_{\text{calc}} \rangle$ and δ_{exp} : $\Delta\delta = \langle \delta_{\text{calc}} \rangle - \delta_{\text{exp}}$. The

results for $\Delta\delta$ are shown in the Supporting Information. For the simulation of $A\beta_{1-40}$ with ffG43a2, it becomes obvious that large deviations between $\langle \delta_{\text{calc}} \rangle$ and δ_{exp} ($|\Delta\delta| > 1$ ppm) occur for almost all residues between residues 7 and 35. Particularly striking is the overestimation of $\langle \delta_{\text{calc}} \rangle$ between residues 13 and 23, whereas for the other residues, we observe an alternation of over- and underestimation of $\langle \delta_{\text{calc}} \rangle$, for example, from residues 7 to 12 and from 28 to 35.

Since $C\alpha$ atoms experience a relative upfield shift when the residue in question is incorporated into an α - or π -helix^{20,69} or a turn region,²⁰ we conclude that in the regions with $\Delta\delta > 1$ ppm, one of these secondary structures is overstabilized by ffG43a2. Indeed, the DSSP plot in Figure 2a shows a rather stable α -helix between residues 13 and 23 in $A\beta_{1-40}$. From ^{15}N relaxation data, a structural propensity for π -helix was predicted for residues 11–15 in $A\beta_{1-40}$. However, from the comparison of the $C\alpha$ shift results, it becomes obvious that ffG43a2 overestimates the N-terminal helical stability in $A\beta_{1-40}$. This helical stability leads to a reduction of the conformational flexibility of the $A\beta$ peptides, as the high population of the first five clusters from the ffG43a2 simulations revealed. A too-small computed $C\alpha$ shift is indicative of an overstabilization of β structure as $C\alpha$ protons experience a relative downfield shift when incorporated into a β -sheet.²⁰ The alternation of too-high and too-low shifts between residues 7–12 and 28–35 is thus a result of the overestimation of successive turn and β conformations, respectively. This conclusion is underpinned by the DSSP plot in Figure 2a.

In summary, ffG43a2 does not provide a satisfactory model for the conformational dynamics of $A\beta_{1-40}$. For $A\beta_{1-42}$, the

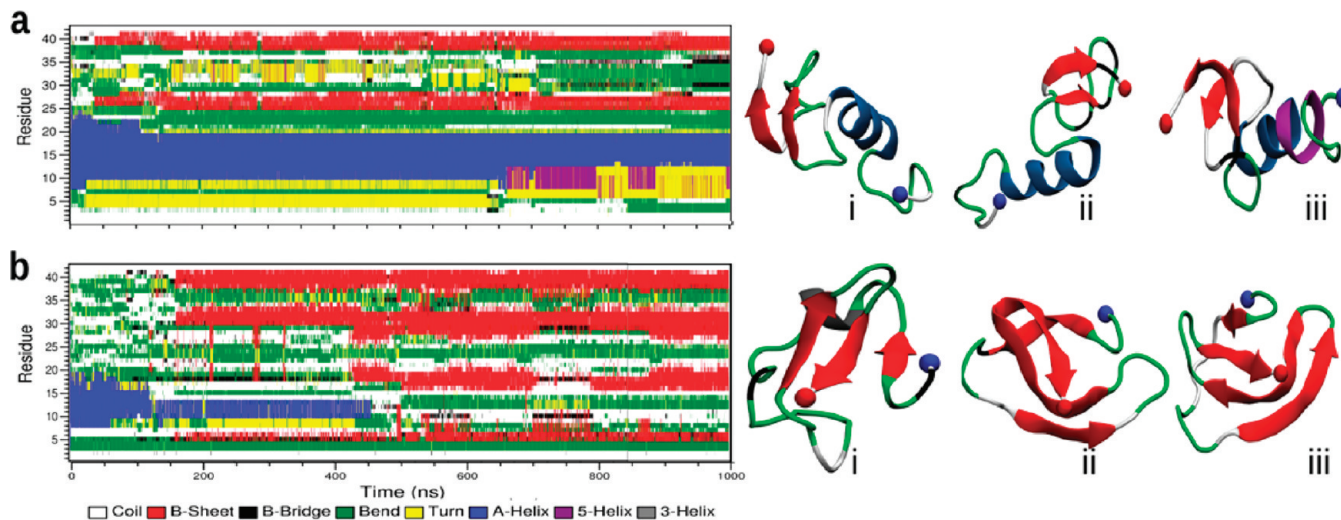


Figure 7. DSSP plots for secondary structure transitions in $\text{A}\beta_{1-42}^0$ with positively charged histidine residues during 1 μs MD simulations using the GROMOS forcefields (a) ffG43a2 and (b) ffG53a6. Structures are shown as obtained at simulation times of (i) 300 ns, (ii) 600 ns, and (iii) 1 μs . See Figure 3 for explanation of colors.

ffG43a2 result is better, especially for the C-terminal part from residue 17 onward, for which most $|\Delta\delta|$ values are <1 ppm. However, for residues 5–16, we observe an overstabilization of the N-terminal π -helix (Figure 4a), leading to $\Delta\delta > 1$ ppm in this region. According to our NMR shift analysis, ffG53a6 provides a good description for both $\text{A}\beta_{1-40}$ and $\text{A}\beta_{1-42}$. Most of the $|\Delta\delta|$ values are <1 ppm. Noteworthy exceptions are residue 22 in $\text{A}\beta_{1-40}$ and residues 6, 12, and 30 in $\text{A}\beta_{1-42}$, for which the β content is slightly overestimated. Our comparison between experimental and simulated chemical shifts is of similar performance as the same kind of analysis in ref 16, in which the simulated shifts were obtained from replica exchange MD simulations of $\text{A}\beta_{1-40}$ and $\text{A}\beta_{1-42}$ using the AMBER99SB force field⁷⁰ with implicit solvation. The representative structures obtained by Yang and Teplow also show similarities to the most important cluster structures, which we obtained with ffG53a6.

In summary, from the comparison between calculated and experimental chemical shifts, we can conclude that ffG53a6 is better able to model the intrinsically disordered $\text{A}\beta$ peptide than ffG43a2, which overestabilizes the helical state in the N-terminal half of the sequence and underestimates the overall conformational flexibility of the peptide. This finding is contrary to the performance of ffG43a2 and ffG53a6 for folded proteins, in which ffG43a2 was found to be better able to maintain folded structures and generally provides a good balance between helical and β folds.⁷¹ The superiority of ffG53a6 for modeling $\text{A}\beta$ may be due to the fact that this force field was solely parametrized to reproduce the free enthalpies of hydration and apolar solvation for a range of compounds.⁵⁴

The relative free enthalpy of solvation between polar and apolar environments is a key determinant in many biomolecular processes of interest, such as protein folding and aggregation or membrane formation and transport over membranes. Thus, the folded protein state in ffG53a6 results from the choice of the parameter set and not vice versa. In a recent study, it was shown that the common protein force fields (ffG53a6 was not included) are generally able to correctly predict the rate of folding and the structure of the native state.⁷² The folding mechanism and the properties of the unfolded state, however, were found to depend substantially on the choice of force field. This finding, as well as other force field studies for $\text{A}\beta$

peptides,¹⁵ demonstrate the need for proper benchmarking of the protein force fields for unfolded and intrinsically disordered proteins.

3.5. Influence of Histidine Protonation on the Secondary Structure of $\text{A}\beta_{1-42}$. The protonation states of the three histidine residues in $\text{A}\beta$ (His6, His13 and His14) have been reported to affect its aggregation via a pH-dependent effect on charge distribution and binding of metal ions.⁷³ Histidine residues have been indicated as sensitizing the peptide to the binding of transition metal ions, and $\text{A}\beta$ mutants replacing His with other residues have been demonstrated as insensitive to the aggregation-promoting influence of Cu^{2+} and Zn^{2+} .^{14,23,25,73} We performed two 1 μs MD simulations using the ffG43a2 and ffG53a6 force fields with His6, His13, and His14 of $\text{A}\beta_{1-42}$ protonated on both imidazolyl nitrogen atoms as against the previous simulations in which only the delta nitrogen atoms were protonated. Protonating both imidazolyl nitrogen atoms results in a change in the net charge of $\text{A}\beta_{1-42}$ from 3– to zero. We thus use $\text{A}\beta_{1-42}^{3-}$ and $\text{A}\beta_{1-42}^0$ in the current discussion to refer respectively to $\text{A}\beta_{1-42}$ with one and two histidine imidazolyl nitrogen atoms protonated.

The effect of histidine protonation on the secondary structure is shown by the DSSP plots in Figure 7. We observe a stabilization of the N-terminal α -helix for both force fields but to a much higher degree in the simulation with ffG43a2. With ffG43a2, $\text{A}\beta_{1-42}^0$ samples an α -helix at Ser8-Phe19, compared with a less compact π -helix at His6-Lys16 sampled by $\text{A}\beta_{1-42}^{3-}$. With ffG53a6, the N-terminal helix was sustained only during the first half of the simulation, during which time a persistent reduction in helical content was observed, which correlates roughly with an increase in the β content. This sharply contrasts with the simulation of $\text{A}\beta_{1-42}^{3-}$ using the same force field, in which the N-terminal helix promptly collapsed, first into disordered states and later sampling β -sheet conformations. This strongly suggests an N-terminal stabilizing function originating from the positively charged histidine residues. Furthermore, the DSSP plots and structures for $\text{A}\beta_{1-42}^0$ in Figure 7 also reveal for both force fields a higher number of β -sheets compared with $\text{A}\beta_{1-42}^{3-}$. The influence of the net charge on $\text{A}\beta_{1-40}$ aggregation was investigated by Guo et al. in which

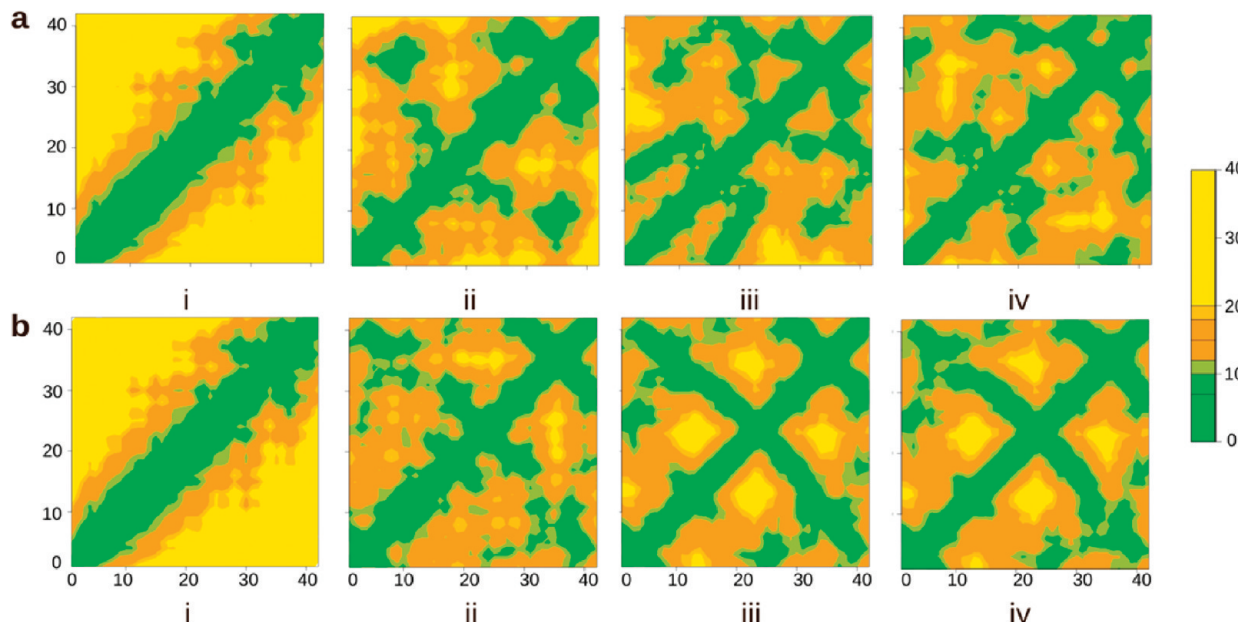


Figure 8. C_α distance maps comparing $A\beta_{1-42}$ with histidine residues simulated either as (a) neutral ($A\beta_{1-42}^{3-}$) or (b) protonated ($A\beta_{1-42}^0$) using the GROMOS forcefield ffG53a6. The distance maps are shown for structures collected at 0 ns, 300 ns, 600 ns, and 1 μ s. The distance scale is in angströms, and both axes of the maps indicate the residue index from 1 through 42.

the charge was modulated by severally mutating histidine, aspartic acid, and glutamic acid residues into alanine.²⁵ They reported a statistically significant correlation of 0.87 between net molecular charge and aggregation. For $A\beta_{1-42}$, a higher aggregation was reported at pH 5.8 than at pH 7.4, concurrently with a higher neurotoxicity, suggesting a correlation between pH-dependent aggregate formation and pathogenesis.⁷⁴

In the above cited experimental works, reduction of excess $A\beta$ charge was achieved by different means, either using point mutations or by employing an acidic pH. We achieved the same charge reduction by directly selecting histidine protonation states to correspond to an acidic pH ($4 < \text{pH} < 7$). One way to explain the increased β -sheet formation (and thus the experimentally observed extent and rate of aggregation) is by considering the effect of protonating the three histidine residues in changing the net charge from 3 $-$ to zero in the helix-forming N-terminal region spanning residues Asp1–Asp23. This local N-terminal charge removal leads to a reduction in electrostatic repulsion and, as a result, a stabilization of the helix.

We generated distance maps for the C_α atoms for structures collected at 0 ns, 300 ns, 600 ns and 1 μ s for both $A\beta_{1-42}^{3-}$ and $A\beta_{1-42}^0$ simulated with ffG53a6 as presented in Figure 8. The distance maps at time zero are typical of a helical structure, especially in the first two-thirds of the peptide. At 300 ns, His13 and His 14 form interresidue contacts with residues between Phe20 and Ala30 in both $A\beta_{1-42}^{3-}$ and $A\beta_{1-42}^0$ (Figure 8a,ii and b,ii). In $A\beta_{1-42}^0$, these interactions also involve possible side chain contacts with amino acid residues in the C-terminal region, leading to the N-terminal helix being sustained in this structure. His6 in $A\beta_{1-42}^0$ is also considerably involved in interactions, especially with Ala30–Ala42, which is likely to be important for the initialization of C-terminal β -strand formation.

These interactions involving histidine residues are much less observed in $A\beta_{1-42}^{3-}$ (Figure 8a). Instead, the N- and C-terminal

segments avoid interacting with each other in $A\beta_{1-42}^{3-}$, which is likely a consequence of charge incompatibility between the hydrophobic C-terminal and the predominantly hydrophilic N-terminal. The distance maps for $A\beta_{1-42}^{3-}$ starting with the 300 ns plot exhibit a pattern suggestive of disordered structures and limited β -sheet. The net charge removal when moving from $A\beta_{1-42}^{3-}$ to $A\beta_{1-42}^0$ thus promotes hydrophobic interactions between the two terminal sections, thereby significantly increasing β -sheet formation. This is an important driving force for the fast aggregation kinetics observed for the amyloid peptide at acidic pH,^{22–24} which should be further enhanced from reduction in electrostatic repulsion between $A\beta_{1-42}^{3-}$ molecules. This result agrees with the observation that electrostatic repulsion prevents $A\beta$ aggregation.²⁵

3.6. $A\beta_{1-42}$ /D3 Interaction Study. From the 100 ns MD simulation of D3, we observed that the conformational space is dominated by the structure shown in Figure 9a. D3 adopts an extended conformation that results from an attempt to minimize electrostatic repulsion among its five arginine residues. We employed this structure for our subsequent simulations investigating D3 binding to $A\beta_{1-42}$. For $A\beta_{1-42}$, we selected three different structures from the 1.5 μ s MD simulation with ffG43a2, making sure that helical, β -strand, and coil secondary structures were adequately represented (Figure 9b–d). Each of the $A\beta_{1-42}$ structures was paired with D3 with the aid of the oligomer-generation procedure recently implemented into GMIN and optimized during 500 basin-hopping steps.⁴⁹ We generated 2000 binary complexes per $A\beta$ starting structure, giving rise to a total of 6000 $A\beta_{1-42}$ /D3 complexes. From these, 100 complexes were selected for further investigation using 10 ns MD simulations. The selection procedure was based on an energy threshold, distance cutoff, and a criterion requiring that the three $A\beta_{1-42}$ starting structures are about equally represented in the selected complexes. Backbone rmsd values indicate a strong binding between the two peptides sustained for the duration of the MD simulations (data not shown).

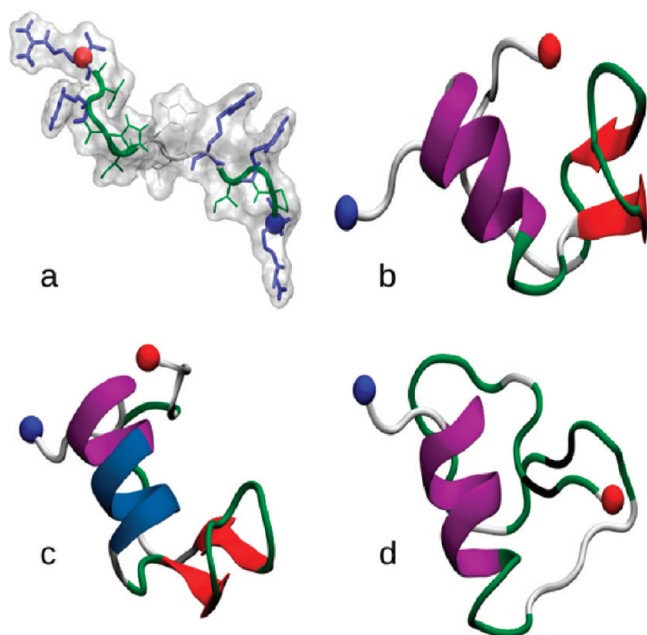


Figure 9. (a) The most favored structure of D3, obtained after clustering the structures sampled in a 100 ns MD simulation at 300 K with arginine residues shown in blue licorice representation. This D3 structure was used to study its binding to $\text{A}\beta_{1-42}$. For the generation of $\text{A}\beta_{1-42}/\text{D3}$ complexes, $\text{A}\beta_{1-42}$ structures collected at (b) 713, (c) 817, and (d) 888 ns in the 1.5 μs MD simulation (ffG43a2, $\text{A}\beta_{1-42}^{3-}$) were selected.

We then decomposed the interaction energies, composed of the Coulombic and Lennard-Jones (LJ) contributions, into interresidue contributions for all $\text{A}\beta_{1-42}/\text{D3}$ residue pairs. This approach yields 42×12 interaction energies, which were time-averaged over the 100 simulated systems and plotted in Figure 10. The result of this analysis shows that the interaction is mediated by strong electrostatic attraction between arginine-

rich D3 and $\text{A}\beta_{1-42}$, since the strongest interactions are obtained for the negatively charged aspartic and glutamic residues in $\text{A}\beta_{1-42}$. In addition, comparing Coulombic and LJ contributions, we observed much higher Coulombic contributions (data not shown). The results in Figure 10 further show that the binding of D3 to the N-terminal segment of $\text{A}\beta_{1-42}$ is more favored compared with the C-terminal segment (apart from the negatively charged C-terminus Ala42-COO^-). The negatively charged amino acid residues Asp7, Glu11, Glu22, and Asp23 and the negatively charged C-terminus are the $\text{A}\beta_{1-42}$ residues with the lowest interaction energies and are therefore most crucial in mediating the binding of arginine-rich D3 to $\text{A}\beta_{1-42}$. The N-terminal positive charge next to residue Asp1 diminishes the interaction of this $\text{A}\beta_{1-42}$ residue with D3. D3 favors binding to the N-terminal segment of $\text{A}\beta_{1-42}$ with its positively charged residues Arg1, Arg3, Arg5, and Arg10.

All three positively charged residues of $\text{A}\beta_{1-42}$ (Arg5, Lys16 and Lys28) are avoided by D3's positively charged residues, as evidenced by repulsive interaction energies in Figure 10. Arg1 of D3 exhibits the strongest attraction to $\text{A}\beta_{1-42}$, interacting with both the C-terminus and the N-terminal negatively charged residues. This strong interaction is due to the N-terminal positive charge next to Arg1, whereas the C-terminal negative charge reduces the interaction of Arg12 of D3 with $\text{A}\beta_{1-42}$. Our interaction analysis thus reveals that the electrostatically driven association brings D3 to the local vicinity of the N-terminal half of $\text{A}\beta_{1-42}$, which includes the central hydrophobic core $^{17}\text{LVFFA}^{21}$. This suggests that D3 prevents the aggregation of $\text{A}\beta_{42}$ into toxic β -sheets by shielding this amyloid-aggregation nucleating sequence.

We then investigated the effect of D3 binding on the structure of the $\text{A}\beta_{1-42}$ monomer. We calculated the time averaged fractional secondary structure units for $\text{A}\beta$ in the $\text{A}\beta_{1-42}/\text{D3}$ complexes for each of the 10 ns MD simulations and averaged these values over the 100 systems. We then compared the results with the secondary structure contributions sampled in three separate 335 ns MD simulations, which were initiated with the $\text{A}\beta_{1-42}$ structures (in the absence of D3) used for the generation of $\text{A}\beta_{1-42}/\text{D3}$ complexes (Figure 9b–d). The results of this analysis are listed in Table 2. The overall

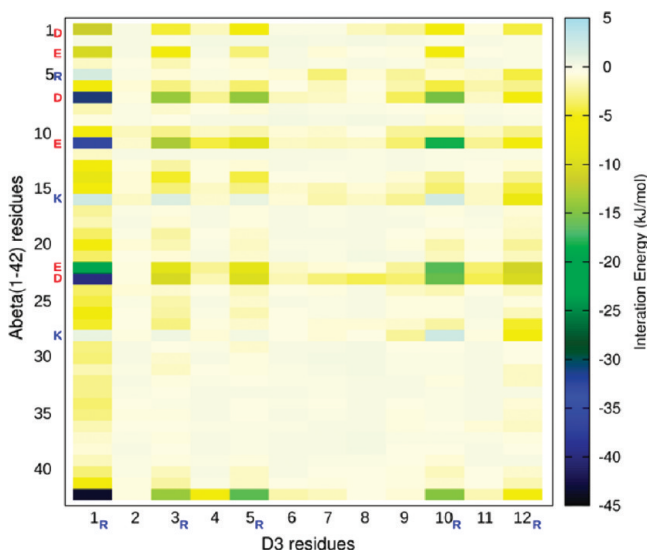


Figure 10. Energy matrix showing how strongly individual D3 residues interact with $\text{A}\beta_{1-42}$ residues. The energy scale is in kilojoules per mole, and the values represent the sum of Coulombic and Lennard-Jones contributions averaged over 10 ns and 100 MD simulations of $\text{A}\beta_{1-42}/\text{D3}$ complexes.

Table 2. Time-Averaged Secondary Structure Contributions (percent) in $\text{A}\beta_{1-42}$ Calculated from Three 335 ns MD Simulations of $\text{A}\beta_{1-42}$ and from 100 Individual 10 ns MD Simulations of $\text{A}\beta_{1-42}/\text{D3}$ Complexes^a

secondary structure	$\text{A}\beta_{1-42}$ (%)	$\text{A}\beta_{1-42}/\text{D3}$ (%)
coil	35.1	37.7
beta	11.5	2.2
bend	18.0	24.0
turn	9.3	13.0
helix	26.1	20.5

^aAll simulations employed ffG43a2.

effect of D3 on $\text{A}\beta_{1-42}$ involves a significant decrease in β -sheet and helical contents and an increase in coil, turn, and bend, suggesting that the binding of D3 to $\text{A}\beta_{1-42}$ induces a conversion of $\text{A}\beta$ β -strand and helices into random coil states. The destruction of β -sheet in $\text{A}\beta_{1-42}$ monomer probably provides an explanation for the amyloid aggregation inhibition observed both in vitro⁴⁴ and in vivo.^{45,46} We are currently investigating the interaction of the D-peptide with $\text{A}\beta_{1-42}$.

oligomers, the outcome of which we believe should further extend our understanding of the antiamyloid mechanism of D3.

4. CONCLUSIONS

Using explicit solvent MD simulations on the microsecond time scale and two GROMOS96 force fields, we investigated different influences affecting the secondary structure of the A β peptide. We conducted a comparative study of A β_{1-40} and A β_{1-42} and also present a perspective on the intramolecular effects of the histidine protonation state on A β_{1-42} , explaining how this leads to the experimentally observed increase in aggregation kinetics at acidic pH.^{22–25} Using the insights afforded by A β conformational studies, we proceeded to investigate the reported antiamyloid properties of D3 using a combination of a global optimization method and MD simulations.

Our simulation results revealed that both peptides are mainly unstructured in the first 10 N-terminal residues. However, A β_{1-40} is more disordered in this region than A β_{1-42} , which also samples either a π -helix or β -sheet in the N-terminal residues. The β -sheet-rich self-recognition motif $^{16}\text{KLVFF}^{20}$ was sampled in both peptides in our simulations but to a higher degree in A β_{1-42} . Both force fields reveal a loss of the C-terminal helix for both peptides, replaced by random coil and β -sheets. We observed the Gly37-Gly38 hinge structure in A β_{1-42} , which was identified as an important feature distinguishing A β_{1-42} from its C-terminal truncated relative.^{63,64}

To validate the force field models, we calculated NMR chemical shifts using CAMSHIFT⁶⁸ and compared them to experimentally determined chemical shifts.⁶⁷ For the ffG53a6 simulations of A β_{1-40} and A β_{1-42} , we found that they converge toward sampling an ensemble that is representative of the experimental data after 500 ns of simulation time. The ffG43a2 simulations, however, fail to completely reproduce the experimental NMR chemical shifts. The largest deviations were observed for the N-terminal half of A β_{1-40} and A β_{1-42} , for which ffG43a2 predicts a rather stable α - and π -helix, respectively. The comparison between calculated and experimental chemical shifts allows us to conclude that in this region, ffG43a2 overestimates the stability of the N-terminal helix and generally underestimates the conformational flexibility of the A β peptides.

We further studied the effect of protonation of the three histidine residues in A β_{1-42} , which reduces the total peptide net charge from 3– (A β_{1-42}^0) to 0 (A β_{1-42}^0) and induces interactions of the otherwise hydrophilic N-terminal region with the hydrophobic C-terminal region. This significantly increased the β -sheet content in A β_{1-42}^0 . We suggest this effect as an important driving force for the fast aggregation kinetics reported for the amyloid peptide at acidic pH via a reduction in intramolecular electrostatic repulsion.²⁵

Finally, using a combination of a global optimization method and MD simulations, we studied the binding of D3 to A β_{1-42} and identified attractive electrostatic forces as the driving force for their interaction. Four negatively charged residues in the N-terminal region of A β_{1-42} serve as binding sites for D3. Analysis of the effect of binding on the secondary structure of A β_{1-42} produced a pattern that agreed with the previously reported amyloid-inhibiting effect of D3 on A β_{1-42} .^{44–46} We observed a significant reduction in β -sheet and helical contents of A β_{1-42} attended by an increase in coil. We consider this as explanatory (at least in part) for the reported antiamyloid properties of D3 on A β_{1-42} peptide.

■ ASSOCIATED CONTENT

5 Supporting Information

rmsd values between calculated and experimental NMR chemical shifts plotted against time; the deviation between time-averaged calculated and experimental NMR chemical shifts plotted against A β residue numbers; information about our calculations of $^3J_{\text{HNH}\alpha}$ coupling constants; rmsd values between calculated and experimental $^3J_{\text{HNH}\alpha}$ coupling constants plotted against time; time-averaged $^3J_{\text{HNH}\alpha}$ coupling constants computed from our MD simulations plotted against the corresponding experimental values. This material is available free of charge via the Internet at <http://pubs.acs.org>.

■ AUTHOR INFORMATION

Corresponding Author

*Phone: +49 2461 613670. Fax: +49 2461 618766. E-mail: b.strodel@fz-juelich.de.

Notes

The authors declare no competing financial interest.

■ ACKNOWLEDGMENTS

We gratefully acknowledge the Jülich Supercomputing Centre for providing and maintaining the computing resources used in this work (computing time Grant JISB32). We thank Prof. Michael G. Zagorski and Dr. Nikolas G. Sgourakis for providing us with the experimentally determined chemical shifts and J -coupling data, respectively. We gratefully acknowledge Prof. Dieter Willbold, Dr. Susanne Aileen Funke, and Dr. Philipp Neudecker for helpful and stimulating discussions.

■ REFERENCES

- (1) Tomaselli, S.; Esposito, V.; Vangone, P.; van Nuland, N. A.; Bonvin, A. M.; Guerrini, R.; Tancredi, T.; Temussi, P. A.; Picone, D. *ChemBioChem* **2006**, *7*, 257–267.
- (2) Selkoe, D. J. *Physiol. Rev.* **2001**, *81*, 741–766.
- (3) Lambert, M. P.; Barlow, A. K.; Chromy, B. A.; Edwards, C.; Freed, R.; Liosatos, M.; Morgan, T. E.; Rozovsky, I.; Trommer, B.; Viola, K. L.; et al. *Proc. Natl. Acad. Sci. U.S.A.* **1998**, *95*, 6448–6453.
- (4) Haass, C.; Schlossmacher, M. G.; Hung, A. Y.; Vigo-Pelfrey, C.; Mellon, A.; Ostaszewski, B. L.; Lieberburg, I.; Koo, E. H.; Schenk, D.; Teplow, D. B. *Nature* **1992**, *359*, 322–325.
- (5) Crescenzi, O.; Tomaselli, S.; Guerrini, R.; Salvadori, S.; D'Ursi, A. M.; Temussi, P. A.; Picone, D. *Eur. J. Biochem.* **2002**, *269*, 5642–5648.
- (6) Shao, H.; Jao, S.; Ma, K.; Zagorski, M. G. *J. Mol. Biol.* **1999**, *285*, 755–773.
- (7) Coles, M.; Bicknell, W.; Watson, A. A.; Fairlie, D. P.; Craik, D. J. *Biochemistry* **1998**, *37*, 11064–11077.
- (8) Sticht, H.; Bayer, P.; Willbold, D.; Dames, S.; Hilbich, C.; Beyreuther, K.; Frank, R. W.; Rosch, P. *Eur. J. Biochem.* **1995**, *233*, 293–298.
- (9) Danielsson, J.; Andersson, A.; Jarvet, J.; Graslund, A. *Magn. Reson. Chem.* **2006**, *44*, S114–S121.
- (10) Reddy, G.; Straub, J. E.; Thirumalai, D. *J. Phys. Chem. B* **2009**, *113*, 1162–1172.
- (11) Tarus, B.; Straub, J. E.; Thirumalai, D. *J. Mol. Biol.* **2008**, *379*, 815–829.
- (12) Chebaro, Y.; Mousseau, N.; Derreumaux, P. *J. Phys. Chem. B* **2009**, *113*, 7668–7675.
- (13) Melquiond, A.; Dong, X.; Mousseau, N.; Derreumaux, P. *Curr. Alzheimer Res.* **2008**, *5*, 244–250.
- (14) Raffa, D. F.; Rauk, A. *J. Phys. Chem. B* **2007**, *111*, 3789–3799.
- (15) Sgourakis, N. G.; Yan, Y.; McCallum, S. A.; Wang, C.; Garcia, A. E. *J. Mol. Biol.* **2007**, *368*, 1448–1457.
- (16) Yang, M.; Teplow, D. B. *J. Mol. Biol.* **2008**, *384*, 450–464.

- (17) Takeda, T.; Klimov, D. K. *J. Phys. Chem. B* **2009**, *113*, 6692–6702.
- (18) Vitalis, A.; Cafisch, A. *J. Mol. Biol.* **2010**, *403*, 148–165.
- (19) Sgourakis, N. G.; Merced-Serrano, M.; Boutsidis, C.; Drineas, P.; Du, Z.; Wang, C.; Garcia, A. E. *J. Mol. Biol.* **2011**, *405*, 570–583.
- (20) Wood, G. P. F.; Rothlisberger, U. *J. Chem. Theory Comput.* **2011**, *7*, 1552–1563.
- (21) Yan, Y.; Wang, C. *J. Mol. Biol.* **2006**, *364*, 853–862.
- (22) Burdick, D.; Soreghan, B.; Kwon, M.; Kosmoski, J.; Knauer, M.; Henschen, A.; Yates, J.; Cotman, C.; Glabe, C. *J. Biol. Chem.* **1992**, *267*, 546–554.
- (23) Atwood, C. S.; Moir, R. D.; Huang, X.; Scarpa, R. C.; Bacarra, N. M.; Romano, D. M.; Hartshorn, M. A.; Tanzi, R. E.; Bush, A. I. *J. Biol. Chem.* **1998**, *273*, 12817–12826.
- (24) Syme, C. D.; Nadal, R. C.; Rigby, S. E.; Viles, J. H. *J. Biol. Chem.* **2004**, *279*, 18169–18177.
- (25) Guo, M.; Gorman, P. M.; Rico, M.; Chakrabartty, A.; Laurents, D. V. *FEBS Lett.* **2005**, *579*, 3574–3578.
- (26) Ibarreta, D.; Urcelay, E.; Parrilla, R.; Ayuso, M. S. *Ann. Neurol.* **1998**, *44*, 216–222.
- (27) Yates, C. M.; Butterworth, J.; Tennant, M. C.; Gordon, A. J. *Neurochem.* **1990**, *55*, 1624–1630.
- (28) Soto, P.; Griffin, M. A.; Shea, J. E. *Biophys. J.* **2007**, *93*, 3015–3025.
- (29) Scherzer-Attali, R.; Pellarin, R.; Convertino, M.; Frydman-Marom, A.; Egoz-Matia, N.; Peled, S.; Levy-Sakin, M.; Shalev, D. E.; Cafisch, A.; Gazit, E.; et al. *PLoS One* **2010**, *5* (e11101), 1–15.
- (30) Liu, R.; Barkhordarian, H.; Emadi, S.; Park, C. B.; Sierks, M. R. *Neurobiol. Dis.* **2005**, *20*, 74–81.
- (31) Ono, K.; Yoshiike, Y.; Takashima, A.; Hasegawa, K.; Naiki, H.; Yamada, M. *J. Neurochem.* **2003**, *87*, 172–181.
- (32) Schenk, D.; Barbour, R.; Dunn, W.; Gordon, G.; Grajeda, H.; Guido, T.; Hu, K.; Huang, J.; Johnson-Wood, K.; Khan, K.; et al. *Nature* **1999**, *400*, 173–177.
- (33) Bard, F.; Cannon, C.; Barbour, R.; Burke, R. L.; Games, D.; Grajeda, H.; Guido, T.; Hu, K.; Huang, J.; Johnson-Wood, K.; et al. *Nat. Med.* **2000**, *6*, 916–919.
- (34) Tjernberg, L. O.; Naslund, J.; Lindqvist, F.; Johansson, J.; Karlstrom, A. R.; Thyberg, J.; Terenius, L.; Nordstedt, C. *J. Biol. Chem.* **1996**, *271*, 8545–8548.
- (35) Findeis, M. A.; Lee, J. J.; Kelley, M.; Wakefield, J. D.; Zhang, M. H.; Chin, J.; Kubasek, W.; Molineaux, S. M. *Amyloid* **2001**, *8*, 231–241.
- (36) Gordon, D. J.; Sciarretta, K. L.; Meredith, S. C. *Biochemistry* **2001**, *40*, 8237–8245.
- (37) Hochdorffer, K.; Marz-Berberich, J.; Nagel-Steger, L.; Epple, M.; Meyer-Zaika, W.; Horn, A. H.; Sticht, H.; Sinha, S.; Bitan, G.; Schrader, T. *J. Am. Chem. Soc.* **2011**, *133*, 4348–4358.
- (38) Soto, C.; Sigurdsson, E. M.; Morelli, L.; Kumar, R. A.; Castano, E. M.; Frangione, B. *Nat. Med.* **1998**, *4*, 822–826.
- (39) Nerelius, C.; Sandegren, A.; Sargsyan, H.; Raunak, R.; Leijonmarck, H.; Chatterjee, U.; Fisahn, A.; Imarisio, S.; Lomas, D. A.; Crowther, D. C.; et al. *J. Proc. Natl. Acad. Sci. U.S.A.* **2009**, *106*, 9191–9196.
- (40) Blanchard, B. J.; Hiniker, A. E.; Lu, C. C.; Margolin, Y.; Yu, A. S.; Ingram, V. M. *J. Alzheimer's Dis.* **2000**, *2*, 137–149.
- (41) Blanchard, B. J.; Konopka, G.; Russell, M.; Ingram, V. M. *Brain Res.* **1997**, *776*, 40–50.
- (42) Chalifour, R. J.; McLaughlin, R. W.; Lavoie, L.; Morissette, C.; Tremblay, N.; Boule, M.; Sarazin, P.; Stea, D.; Lacombe, D.; Tremblay, P.; et al. *J. Biol. Chem.* **2003**, *278*, 34874–34881.
- (43) Tjernberg, L. O.; Lilliehook, C.; Callaway, D. J.; Naslund, J.; Hahne, S.; Thyberg, J.; Terenius, L.; Nordstedt, C. *J. Biol. Chem.* **1997**, *272*, 12601–12605.
- (44) Wiesehan, K.; Buder, K.; Linke, R. P.; Patt, S.; Stoldt, M.; Unger, E.; Schmitt, B.; Bucci, E.; Willbold, D. *ChemBioChem* **2003**, *4*, 748–753.
- (45) van Groen, T.; Wiesehan, K.; Funke, S. A.; Kadish, I.; Nagel-Steger, L.; Willbold, D. *ChemMedChem* **2008**, *3*, 1848–1852.
- (46) Funke, S. A.; van Groen, T.; Kadish, I.; Bartnik, D.; Nagel-Steger, L.; Brener, O.; Sehl, T.; Batra-Safferling, R.; Moriscot, C.; Schoehn, G.; et al. *ACS Chem. Neurosci.* **2010**, *1*, 639–648.
- (47) Wales, J. D.; Doye, J. P. K. *J. Phys. Chem. A* **1997**, *101*, 5111–5116.
- (48) Wales, D. J.; Scheraga, H. A. *Science* **1999**, *285*, 1368–1372.
- (49) Strodel, B.; Lee, J. W.; Whittleston, C. S.; Wales, D. J. *J. Am. Chem. Soc.* **2010**, *132*, 13300–13312.
- (50) Li, Z.; Scheraga, H. A. *Proc. Natl. Acad. Sci. U.S.A.* **1987**, *84*, 6611–6615.
- (51) Schuettelkopf, A.; van Aalten, D. *Acta Crystallogr.* **2004**, *D60*, 1355–1363.
- (52) van Gunsteren, W. F.; Billeter, S. R.; Eising, A. A.; Hünenberger, P. H.; Krüger, P.; Mark, A. E.; Scott, W. R. P.; Tironi, I. G. *Biomolecular Simulation: The GROMOS96 Manual and User Guide*; Hochschulverlag AG an der ETH Zürich: Zürich, Switzerland; 1996.
- (53) Daura, X.; Mark, A. E.; van Gunsteren, W. F. *J. Comput. Chem.* **1998**, *19*, 535–547.
- (54) Oostenbrink, C.; Villa, A.; Mark, A. E.; van Gunsteren, W. F. *J. Comput. Chem.* **2004**, *25*, 1656–1676.
- (55) Hess, B.; Kutzner, C.; van der Spoel, D.; Lindahl, E. *J. Chem. Theory Comput.* **2008**, *4*, 435–447.
- (56) GMIN: A program for basin-hopping global optimization. Wales, D. J. <http://www.wales.ch.cam.ac.uk/software.html>.
- (57) Mortenson, P. N.; Wales, D. J. *J. Chem. Phys.* **2001**, *114*, 6443–6454.
- (58) Strodel, B.; Wales, D. J. *J. Chem. Theory Comput.* **2008**, *4*, 657–672.
- (59) MacKerell, A. D. Jr.; Bashford, D.; Bellott, M.; Dunbrack, R. L. Jr.; Evanseck, J. D.; Field, M. J.; et al. *J. Phys. Chem. B* **1998**, *102*, 3586–3616.
- (60) Kabsch, W.; Sander, C. *Biopolymers* **1983**, *22*, 2577–2637.
- (61) Daura, X.; Gademann, K.; Jaun, B.; Seebach, D.; van Gunsteren, W.; Mark, A. *Angew. Chem., Int. Ed.* **1999**, *38*, 236–240.
- (62) Humphrey, W.; Dalke, A.; Schulten, K. *J. Mol. Graph.* **1996**, *14*, 33–38.
- (63) Urbanc, B.; Cruz, L.; Yun, S.; Buldyrev, S. V.; Bitan, G.; Teplow, D. B.; Stanley, H. E. *Proc. Natl. Acad. Sci. U.S.A.* **2004**, *101*, 17345–17350.
- (64) Yun, S.; Urbanc, B.; Cruz, L.; Bitan, G.; Teplow, D. B.; Stanley, H. E. *Biophys. J.* **2007**, *92*, 4064–4077.
- (65) Bitan, G.; Vollers, S. S.; Teplow, D. B. *J. Biol. Chem.* **2003**, *278*, 34882–34889.
- (66) Bitan, G.; Kirkadze, M. D.; Lomakin, A.; Vollers, S. S.; Benedek, G. B.; Teplow, D. B. *Proc. Natl. Acad. Sci. U.S.A.* **2003**, *100*, 330–335.
- (67) Hou, L.; Shao, H.; Zhang, Y.; Li, H.; Menon, N. K.; Neuhaus, E. B.; Brewer, J. M.; Byeon, I. J.; Ray, D. G.; Vitek, M. P.; et al. *J. Am. Chem. Soc.* **2004**, *126*, 1992–2005.
- (68) Kohlhoff, K. J.; Robustelli, P.; Cavalli, A.; Salvatella, X.; Vendruscolo, M. *J. Am. Chem. Soc.* **2009**, *131*, 13894–13895.
- (69) Dalgarno, D. C.; Levine, B. A.; Williams, R. J. *Biosci. Rep.* **1983**, *3*, 443–452.
- (70) Hornak, V.; Abel, R.; Okur, A.; Strockbine, B.; Roitberg, A.; Simmerling, C. *Proteins* **2006**, *65*, 712–725.
- (71) Matthes, D.; de Groot, B. L. *Biophys. J.* **2009**, *97*, 599–608.
- (72) Piana, S.; Lindorff-Larsen, K.; Shaw, D. E. *Biophys. J.* **2011**, *100*, L47–L49.
- (73) Pagel, K.; Seri, T.; von Berlepsch, H.; Griebel, J.; Kirmse, R.; Bottcher, C.; Koks, B. *ChemBioChem* **2008**, *9*, 531–536.
- (74) Su, Y.; Chang, P. T. *Brain Res.* **2001**, *893*, 287–291.